Spatiotemporal Characteristics and Trend Analysis of two Evapotranspiration-based droughts products and their mechanisms in Sub-Saharan Africa

Isaac Kwesi Nooni[1,2], Daniel Fiifi T. Hagan[2], Guojie Wang[2]*, Waheed Ullah[2], Shijie Li[2], Jiao Lu[2], Asher Samuel Bhatti[2], Xiao Shi[2,3], Dan Lou[2], Nana Agyemang Prempeh[4], Kenny T.C. Lim Kam Sian[1,5], Mawuli Dzakpasu[6], Solomon Obiri Yeboah Amankwah[2], Chenxia Zhu[2]

nooni25593@alumni.itc.nl (I.K.N); dans7messiah@nuist.edu.cn (D.F.T.H) gwang@nuist.edu.cn(G.W); waheed.wama@nuist.edu.cn (W.U); lishijie@nuist.edu.cn(S.L.); jiao_lu@nuist.edu.cn (JL); ashersamu@gmail.com (A.S.B); 18801580429@163.com(X.S); loudan711@163.com (D.L); agyemang.prempeh@uenr.edu.gh (N.A.P); kennylim@nuist.edu.cn (K.T.C.L.K.S) mawuli_dzkps@yahoo.com.au (M.D); 20195111003@nuist.edu.cn (S.O.Y.A.); zhuchenxia@nuist.edu.cn (Z.C).

[1]Binjiang College, Nanjing University of Information Science & Technology, No.333 Xishan Road, Wuxi 214105, China

[2]Collaborative Innovation Center on Forecast and Evaluation of Meteorological Disasters, School of Geographical Sciences, Nanjing University of Information Science & Technology, Nanjing 210044, China

[3]Jiangsu Meteorological Bureau, Meteorological Services Center, Nanjing 210008, China

[4]School of Geosciences, Department of Geographic Sciences, University of Energy and Natural Resources, P.O. Box 214, Sunyani-Ghana

[5]College of Atmospheric Sciences, Nanjing University of Information Science and Technology, Nanjing 210044, China

[6]Key Lab of Northwest Water Resources, Environment and Ecology, School of Environmental and Municipal Engineering, Xi'an University of Architecture and Technology, No.13 Yanta Road, Xi'an, 710055, China.

* Correspondence author email: gwang@nuist.edu.cn

Abstract: Drought severity still remains a serious concern across sub-Saharan Africa (SSA) due to the destructive impact on multiple sectors of our society The interannual variability and trends in the changes of self-calibrated Palmer Drought Severity Index based on Penman–Monteith (scPDSIPM) and Thornthwaite (scPDSITH) methods for potential evapotranspiration (PET), precipitation (P) and normalized difference vegetation index (NDVI) anomalies, and sea surface temperature (SST) anomaly were investigated through statistical analysis of modelled and remote sensing data. It is shown that scPDSIPM and scPDSITH differed in the representation of drought characteristics over SSA. The scPDSI and remotely-sensed-based anomalies of P and NDVI showed wetting and drying trends over the period 1980-2012. The trend analysis showed increased drought events in the semi-arid and arid regions of SSA over the same period. A correlation analysis reveals a strong relationship between scPDSI variability and P, and NDVI anomalies for monsoon and pre-monsoon seasons. The correlation analysis of scPDSI variability with SST anomalies indicates significant positive and negative relationships, respectively. This study has demonstrated the applicability of multiple data sources for drought assessment and provides useful information for regional drought predictability and mitigation strategies.

Keywords: Droughts, NDVI, CHIRPS, precipitation anomalies, potential evapotranspiration (PET), self-calibrating Palmer drought severity index, Sub-Saharan Africa

 doi:10.20944/preprints202012.0620.v1

1. Introduction

According to the fifth assessment report (AR5) of Intergovernmental Panel on Climate Change (IPCC), global warming has significantly contributed to the evolution of extreme weather events (such as droughts, floods, heat waves etc.) [1]. The increase in the severity of these weather events has been documented due to their devastating impact on our ecosystem and different sectors of the society [2]. On the other hand, the projected increase in potential future droughts events under the current global warming have been of keen interest to scholars, researchers and the general public [1].

Generally, to depict and monitor drought events, specialised drought indices are used. However, one key question of concern has been about the proxies used to measure these droughts. For instance, some studies have questioned the use of precipitation (P) deficits as a primary reason to depict historical droughts in a warming climate [3-6], particularly, when there is ample evidence of enhanced atmospheric demand under recent global warming. Decrease in P is generally associated with increased temperature (T) (and reduced atmospheric humidity), which enhances potential evapotranspiration (PET), and later intensify dry spells [4-6]. Therefore, the inclusion of or using atmospheric water demand (or PET) to depict droughts events is worthwhile. A review by Mishra and Singh, [7] outlines a lengthy catalog consisting of multiple specialised drought indices highlighting both the concept of atmospheric "supply" and "demand" and how they account for surface warming effect on wet and dry spells.

Although, there is lack of general consensus on the global droughts assessment [8-12], drought indices designed on the basis of the concept of atmospheric "supply" and "demand" has shaped our understanding of drought [3,7,13-15]. So within this context, the self-calibrated Palmer Drought Severity Index (scPDSI), a typical example of such a drought index [12], has been widely used to study drought climatology at global scales [8,9], regional specific studies [15,16] as well as several others [6]. PDSI, by design, is a physical-based drought index that incorporates antecedent P, moisture supply and demand (i.e. potential evaporation (PET)) to account for surface warming effect on wet and dry spells [12].

Several studies have reported intense drying and increased frequency of droughts in many regions across the World [7]. However, the controversy remains in the order of magnitude of dry spells and changes (or trends) in droughts severity. Although several reasons account for this lack of agreement. The choice of PET used remains the most prominent issue. PET computation (a proxy for atmospheric demand) is sensitive to the choice of PET method used [12,17,18]. The different methods of PET estimation are outlined in Mishra and Singh, [7]. Here, we focus on only the Thornthwaite and the Penman–Monteith methods. In most studies, Thornthwaite method has been shown to overestimate drying trends than the Penman-Monteith method and vice-versa [12,17,18]. Nonetheless, the accuracy and rationality of the two PET methods and their application are still under study [6,7,12].

This study attempts to understand the impact of the two PET methods on drought characteristics and trends in the large-scale convective region of sub-Saharan Africa (SSA) (i.e. a region least explored, except in few studies) [19,20]. In addition, the study uses remotely sensed precipitation (P) and vegetation datasets to investigate how these climate variables respond to drought trends in SSA. Furthermore, we explore the interactive effects of sea surface temperature (i.e. El Nino-Southern

Preprints (www.preprints.org) | NOT PEER-REVIEWED | Posted: 24 December 2020 doi:10.20944/preprints202012.0620.v1

Oscillation (ENSO) and Indian Ocean Dipole (IOD)) on droughts trends which coincidently is lacking and have been recommended [19].

Agriculture is the backbone of the overall economic growth of SSA countries. Agriculture does not only contribute to nearly 24-31% of Gross Domestic Product (GDP) of SSA countries but essential for poverty reduction and food security as it employs more than 65% of the workforce [21]. Apart from other constraints to agricultural development in Africa, the SSA agricultural system is vulnerable to patterns and mechanisms of climate change [21]. The spatio-temporal variability of P coupled with high population growth amplifies the region's vulnerability to droughts due to increasing water demands [20]. This in turn comprise the role of agriculture in reducing poverty in the region, hence, the launch of the Malabo Goals 2025 and the 2030 Agenda for Sustainable Development of the Sustainable Development Goal 2 (SDG2) [21].

To the best of our knowledge, only few attempts in SSA have been made to compare long-term drought characteristics and trends using energy-driven drought indices [19,20]. Thus, in a warming climate, a better understanding of drought characteristics, trends and influencing mechanism over SSA is useful within the context of regional predictability and mitigation strategies. Thus, this paper seeks to contribute to existing literature on droughts studies in the region by using state-of-the-art modelled data and satellite products in a region where data availability and quality concerns remains a challenge. The long-term modelled scPDSI based on two PET methods from 1979-2012 across SSA were used to achieve the following objectives; (1) to characterise droughts events (in terms of their frequency, spatial extent and intensity) (2) to quantify the long-term trends in droughts characteristics in space and time and (3) to evaluate some underlying mechanisms of droughts changes across SSA.

The remaining paper is organized as follows: In section 2, we provide a brief description of the different data used. We also summarized the methods and approaches used in this section. The results of the comparison are presented in section 3. Finally, section 4 and 5 discuss the most important study findings and conclusion respectively.

2. Materials and Methods

2.1 Study Area:

Sub-Saharan Africa (SSA) is defined as the vast land mass area south of the Sahara Desert between 15°00′ N to 35°00′S and 14°00′ W to 52°00′E. SSA is boarded to the southeast by the Indian Ocean and west by the Atlantic Ocean (Fig. 1). It has a total area of nearly 24.7 million km^2 (accounting for approximately 81.2% of entire Africa land area. The region straddles the equator with significant number of countries located in both the Northern and Southern Hemispheres.

Generally, the topography, vegetation conditions, oscillation of Intertropical Convergence Zone (ITCZ), and atmospheric processes impact on precipitation (P) variability throughout the hydrological system [22,23]. The elevation of SSA ranges from -360 to 5,861 m above mean sea level (msl) with the highlands located in the eastern and southern parts of the region (Fig. 1a).

The weather pattern shows two clear seasons (the wet and dry seasons) with wide range of climatic features [24]. The tropical wet and dry climate located along the Guinean coast and the equatorial region have elevation <850m above msl. The Savanna climate covers nearly three-quarters (¾) of SSA land mass with elevation ranging from >170 to < 5,861 m above msl. The semi-arid climate (of the Sudano-Saheliean, large parts of Southern Africa and the Horn of Africa have elevation ranges

Preprints (www.preprints.org) | NOT PEER-REVIEWED | Posted: 24 December 2020 doi:10.20944/preprints202012.0620.v1

from >250 to <5,000 m. Arid climates are found in most parts of Southern and Horn of Africa with elevation ranges from >780 to < 5,861m.

The complexity of the topographical features partly explains the high seasonal and interannual variability in P. Fig. 1c-d presents the annual mean and seasonal climatology of precipitation (P) and temperature (T) over the period 1981 to 2017.

Based on Climate Hazard Group Infrared Precipitation with Stations (CHIRPS) dataset, the annual mean P in SSA ranges <30–>300 mm. We observed in Fig. 1c that areas with high elevation (i.e. Ethiopian highlands) or dense vegetation (i.e. Guinea coast, and Congo forested areas) receive significant amount of an annual mean P >150 mm. The Savanna and Sudano-Sahelian belt climate regions receives <120 and <90 mm respectively. Arid regions receive as low as < 30mm of an annual mean P.

On the other hand, based on the European Center for Medium-Range Weather Forecasts (ECMWF) ERA-5 atmospheric reanalysis datasets, the Arid climate regions in southern Africa have annual mean T ranges from 15–<27^{o}C. The semi-arid climate 24->33^{o}C. The tropical wet and dry climate records <27^{o}C (Fig. 1d).

The P and T pattern in the Northern Hemisphere (NH) is generally bimodal (Fig. 1e-f). In the NH, we observe that the P and T seasonality is not synchronous (Fig. 1e-f, blue and red) as increase in P JJA and SON leads to decrease in T respectively. These seasonal characteristics coupled with other factors (explained below) defines the NH monsoon climate.

For example, the western Africa region receives long rains in boreal summer (i.e. June to August (JJA)) and short rains during boreal autumn (September-November (SON)) with peak values in July (Fig. e, blue). The Horn of Africa (HA) region receives mostly long P from boreal spring (i.e. March to May (MAM)) and short P from October to December (OND) (Fig. 1c, red). On the other hand, the Southern Hemisphere (SH) have a unimodal P and T pattern (Fig. e, black) with long rains in austral summer (i.e. December February (DJF).

Under recent warming climate, changes in P and T over space and time are partly induced by local factors such as the heterogeneity of the land surface. According to the 2016 land use land cover (LULC) map from the European Space Agency Climate Change Initiative (ESACCI) [25], grassland and crop lands occupies 17% and 12% respectively mainly along the Sudano-Sahelian belt-Guinea coast (SSG), horn of Africa (HoA), peripherals of large open water bodies, and the eastern southern Africa regions (Fig. 1b), Dense vegetation accounts for nearly 21% and distributed along the Guinean coast, the Congo basin and the equatorial forests regions. Shrubland (covers 11%) are located mainly in the horn of Africa region and southern central Africa regions. Bare land occupies 32% of land area is located mainly in the Sahara Desert (masked out) and parts of southern Africa area. Open water bodies (covers 7.2%) are interspersed and distributed mainly in the equatorial regions and south of the equator. The remaining cover types (covers 1.4%) such as the sparse vegetation, vegetated wetland, buildup areas are interspersed across SSA (Table 1).

Precipitation (P) variability is partly impacted by the interaction with global climate forcing systems such as the El Ni˜no Southern Oscillation (ENSO) and Indian Ocean Dipole (IOD). These teleconnections in space and time is widely reported to explain annual and seasonal P variability in SSA [26].

Preprints (www.preprints.org) | NOT PEER-REVIEWED | Posted: 24 December 2020 doi:10.20944/preprints202012.0620.v1

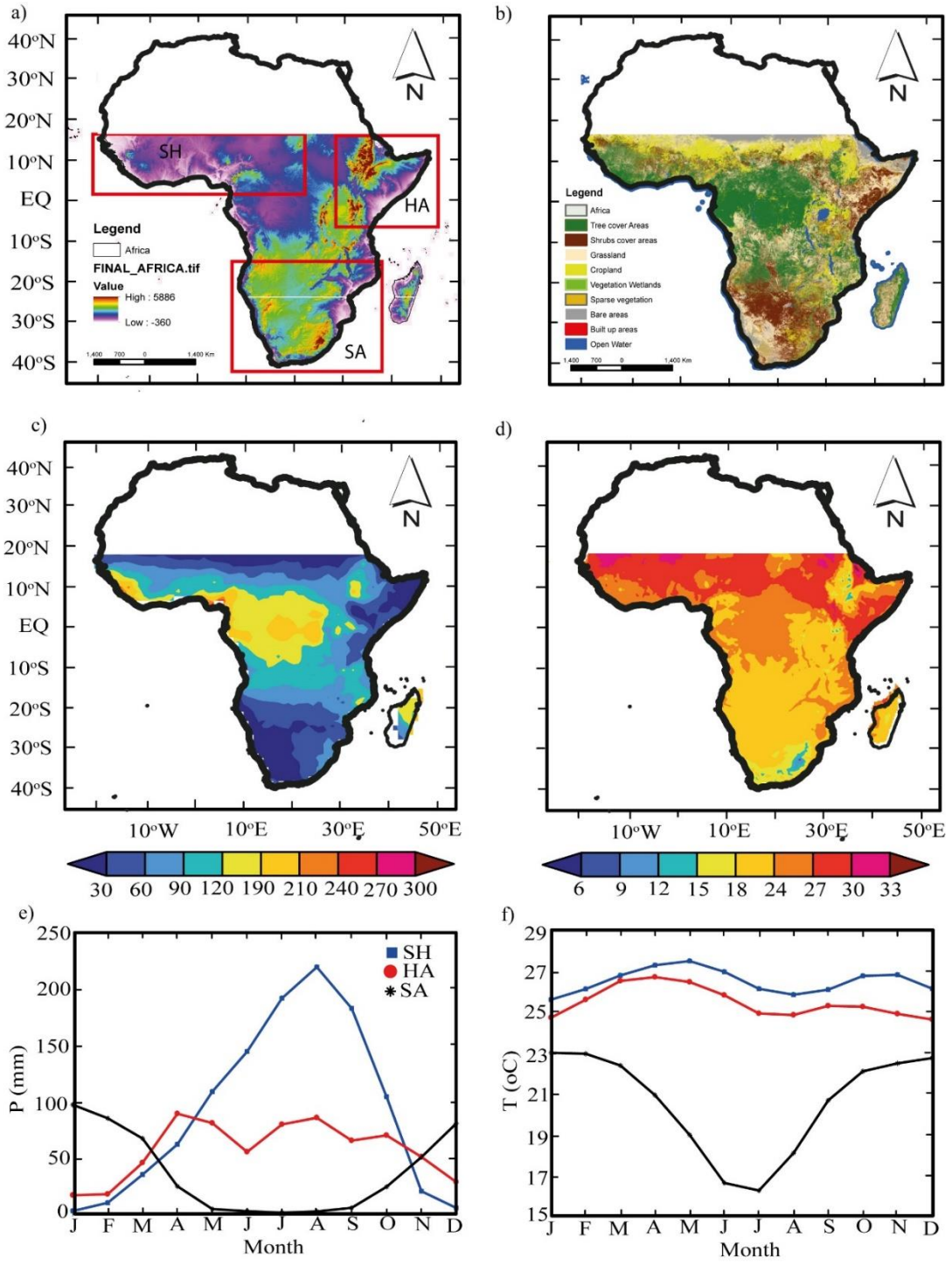

Figure 1. shows the administrative boundary of continental Africa with (a) Topography at 30m resolution acquired from Shuttle Radar Topography Mission (SRTM) digital elevation model (DEM) of National Aeronautics and Space Administration (NASA) [27]. Boxes indicate the three sub-regions used for the spatial averaged analysis: Sudano-Saheliean-Guinean coast (SSG) [5°N-15°N, 5°W-20°E], Horn of Africa (HoA) [5°S-15°N, 30°-52°E], and the southern Africa region (SAR) [32°S-15°S, 8°-32°E]. SSG region used in this paper includes the Sahelian, Sudanian belt and parts of Guinean coast stretch from the Atlantic Ocean to central region along longitudes 20°E. The HoA used here extends from the interior of the Ethiopian and Kenyan highlands to the coast of the Indian Ocean. The SAR includes areas that lie below 15°S. The justification for the selecting the limits of the boxes were based on their

Preprints (www.preprints.org) | NOT PEER-REVIEWED | Posted: 24 December 2020 doi:10.20944/preprints202012.0620.v1

interannual P variations, mean climate and associations with teleconnections [26,28,29] respectively (b) 2016 LULC map at 20m resolution acquired from ESACCI (see Table 1 for details) [25]. (c-d) Spatial distribution of annual average CHIRPS P and ERA-5 T over the period 1981-2017. (e-f) Multi-year (1981–2017) averaged monthly (e) Precipitation (P) (f) Temperature (T).

Table 1. Land Use Land Cover (LULC) types and their respective areal coverage expressed as percentages.

LULC type	Areal coverage (%)
Tree cover	20.70
Shrubland	10.80
grassland	16.60
Cropland	11.80
Vegetated wetlands	0.14
Sparse vegetation	1.050
Bare lands	31.60
Built up	0.20
Open water	7.21
Total	100

Source: ESACCI [25]. Notes that these values include continental Africa.

2.2 Data Description

We briefly describe the specific data sets used in this study.

2.2.1 Drought index Data

The study used self-calibrated Palmer Drought Severity Index (scPDSI) (Palmer 1965) to characterize droughts events in SSA. Many studies have recommended the PDSI as a good proxy for surface soil moisture condition and suitable for drought monitoring [7]. In the design of PDSI, several climatic variables were incorporated to reflect the drying and wetting conditions of an area. So to characterize drought event, we used PDSI datasets downloaded from Princeton website [30].

The PDSI dataset has a global coverage at a 1°x1° spatial resolution and monthly temporal resolution (over the period 1948–2008) [9,31]. Sheffield et al., [31] developed two kinds of PDSI based on the Thornthwaite and the Penman–Monteith algorithms. The climate forcing datasets (i.e. covers 1979-2008) used to produce this scPDSI reflected and captured all forms of anthropogenic activities in the region. Particularly, as within the context of global warming, SSA has experienced several years of land use land cover (LULC). The dataset is publicly available and readers may refer to the developers [9,31] for detailed information about the accuracy, rationality of the input forcing data, choice of baseline period and calculation schemes.

2.2.2 Satellite based Normalized Difference Vegetation Index (NDVI)

To study the spatio-temporal patterns of vegetation greenness and their responses to drying and wetting conditions, the study used Normalized Difference Vegetation Index (NDVI) from Global Inventory Modelling and Mapping Studies (GIMMS) NDVI3g dataset product with a temporal resolution of a 15-day intervals and 1/12-degree spatial resolution processed and archived by the GIMMS group at NASA [32]. The NDVI used in this study spans from 1982 to present. To ensure robustness of long-term trends and variability, the GIMMS group corrected and calibrated the dataset

Preprints (www.preprints.org) | NOT PEER-REVIEWED | Posted: 24 December 2020 doi:10.20944/preprints202012.0620.v1

to minimize sensor effects by using high quality NDVI data from state-of-the art sensors and retrieval algorithms (i.e. Bayesian methods). The algorithm for calculating NDVI is presented in Equation 1.

$$\mathrm{NDVI} = \frac{\mathrm{NIR} - \mathrm{VIS}}{\mathrm{NIR} + \mathrm{VIS}} \quad (1)$$

where NIR denote the near-infrared (NIR) and red (VIS) top-of-atmosphere reflectance.

Generally, NDVI ranges from +1 to -1. But for this study, only vegetated areas were considered from the range of 0.2 – 0.8 pixels values while pixels values <0.12 were masked out to ensure that only NDVI values related to vegetation greenness were captured following Martiny et al. [33]. This means that bare soils and desert areas which correspond to mean pixels values <0.12 and negatives values were excluded. For more details of GIMMS NDVI3g dataset product descriptions, readers are referred to the following references [32].

2.2.3 Climate Hazard Group Infrared Precipitation with Stations (CHIRPS)

We selected CHIRPS products which produces gridded monthly P product from combined in-situ and satellites inputs for monitoring extremes events such as floods, drought or heat waves [34]. The CHIRPS is a semi-global precipitation product and is publically available at the Climate Hazards Group [34] and the International Research Institute climate data library [35] at several temporal resolutions and at 0.05◦ spatial resolution.

However, this study chose the second version of CHIRPS (1981–present) with a spatial resolution of 0.05◦ ranging from 50◦ S to 50◦ N (and all longitudes) at monthly temporal resolution [34,36]. Detailed production of CHIRPS is explained by Funk et al. [34]and CHIRPS is widely used for different applications over several regions of the World [37,38].

2.2.4 Sea Surface Temperature (SST) Indices

In order to study and explain the effect of teleconnections on droughts evolution, we downloaded Indian Ocean Dipole (IOD) and the Ni-no-3.4 (N3.4) sea surface temperature (SST) indices from their respective websites [40,41]. Our study chose monthly time step from the period from January 1979–December 2012 to provide a general picture of the relationship of IOD and El Nino-Southern Oscillation (ENSO) with droughts trends over the region. Ni-no-3.4 (N3.4) originates from Climate Prediction Center (CPC) over 5°N–5°S, 170°–120°W regions. Smith et al. [42] compiles a comprehensive documentation and computation of these datasets.

2.2.5 Other Auxiliary Datasets

To represent the temperature (T) climatology of the region, the study acquired gridded monthly ERA-5 T data aggregated at 0.25 × 0.25° resolution. The ERA-5 T dataset is a global atmospheric reanalysis product produced by ECMWF [39]. In addition, the study used a 20m resolution LULC map acquired from the ESACCI [25] and 30 m Shuttle Radar Topography Mission (SRTM) digital elevation map (DEM) downloaded from the NASA (SRTM) website [27] to visualize the LULC and elevation of the region.

2.3 Methods

2.3.1 Data Preprocessing

Preprints (www.preprints.org) | NOT PEER-REVIEWED | Posted: 24 December 2020 doi:10.20944/preprints202012.0620.v1

Our first step was to pre-process the drought dataset used in this study. For simplicity of presentation, this study used scPDSI_pm and scPDSI_th to represent the PDSI index based on the Penman–Monteith and the Thornthwaite methods respectively.

From the global PDSI dataset, the first preprocessing was to constrain the scPDSI values to the range −10 to 10 values (based on Dai et al., [12] prior to masking the study area. To be able to measure a drought event, we needed to define a drought threshold. Based on literature on PDSI range (see Table 2), we adopted and defined drought events [8,16]. Table 2 provides a classical Palmer [43] classification for wet and dry conditions. So using scPDSI time series per grid, we identified for each grid, scPDSI values below some user defined thresholds. We used −2.0 threshold to denote moderate drought events and −4.0 for more extreme droughts.

In addition, we aggregated the biweekly NDVI data into monthly and then, aggregated into annual and seasonal values over the period 1982-2012 by simple spatial and temporal averages. Also, CHIRPS P grid points covering SSA were extracted and aggregated from monthly to annual and seasonal averages for each year respectively. Lastly, we regridded all the satellite (i.e. CHIRPS P and NDVI) datasets to match the scPDSI datasets resolution using nearest neighbourhood [46,47].

Table 2 Classifications of scPDSI based land wetting and drying

Categories	scPDSI
Extremely dry	≤−4.0
Severely dry	−3.99 to −3.0
Moderately dry	−2.99 to −2.0
Near normal	−1.99 to 1.99
Moderately wet	2.0–2.99
Severely wet	3.0–3.99
Extremely wet	≥4.0

2.3.2 Statistical analysis

Analyses in this study were based on annual and seasonal changes. Different statistical methods were used to compare and analyse the difference among the datasets. For seasonal analysis, we adopted pre-monsoon and monsoon seasons. Thus, we calculated the seasonal mean of the monthly time series (for each pixel) for pre-monsoon (November-December-January-February-March (NDJFMA)) and monsoon season (May-June-July-August-September (MJJASO)) to capture the boreal and austral P regimes in both NH and SH respectively.

Also, in the annual time step, we calculated the spatial mean for each year for each pixel. For inter-annual analysis, the main statistical parameters used in the temporal analysis were means over the period. Afterwards, droughts trends and temporal changes per grid over the period were performed using the Mann–Kendall (M-K) non-parametric statistical test [49,50] and Sen Slope estimator [51] at 0.05 significance level based on World Meteorological Organization (WMO) recommendation and widely used to assess trends in climatological and hydrological time series [52].

To apply the statistical test, we defined two (i.e. the null and alternative) hypothesis for the scPDSI, CHIRPS and, NDVI dataset as follows,

- H_0 = Null hypothesis of trend absence in time series.
- H_1 = Alternative hypothesis of the trend in time series.

Preprints (www.preprints.org) | NOT PEER-REVIEWED | Posted: 24 December 2020 doi:10.20944/preprints202012.0620.v1

The detailed theory and estimation procedure for both M-K and Sen Slope estimator are presented in [52].

In addition, in analysing the interannual variability, the P and NDVI anomalies were calculated based on the spatially averaged annual and seasonal values of each pixel. A negative P and NDVI values denote a drying and vegetative stress and a positive values denote wetting trends and vegetation greening. We also conducted two kinds of correlation analysis to examine precisely and understand the relationships of climatic factors (i.e. P), vegetation condition (i.e. NDVI) and teleconnections (i.e. ENSO and IOD) on wet and dry spells. We computed spatial correlation to analyse their spatial dynamics on scPDSI while for temporal correlation, we conducted a pixel-wise correlation of each variable on annual and seasonal scale to understand the temporal dynamics. All relationships were calculated for the period 1982- 2012.

3. Results

3.1. Spatiotemporal Characteristics of Sub-Saharan Africa (SSA) Droughts

Fig. 2 presents the spatial pattern of drought frequencies of two scPDSI datasets across SSA over the period 1979-2012. Fig. 2a-b show frequencies for moderate drought while Fig. 2c-d presents frequencies for extreme drought. Overall, both scPDSI differed in representing drought frequencies over space. Particularly, areas located in the northwest tips of the SSG, patches north and south of the Congo basin and patches surrounding the Kalahari Desert to the southeast tip of Mozambique (on 18^{o}S-22^{o}S) showed similar agreement in detecting moderate and extreme droughts. However, moderate (extreme) drought occurred more (less) frequently and affected larger (smaller) areas in scPDSI$_{TH}$ relative to scPDSI$_{PM}$ (Fig. 2a-d). On the other hand, disagreement in few areas characterized by complex topography, large water bodies/wetlands and dense vegetation were captured in both scPDSI datasets.

Preprints (www.preprints.org) | NOT PEER-REVIEWED | Posted: 24 December 2020 doi:10.20944/preprints202012.0620.v1

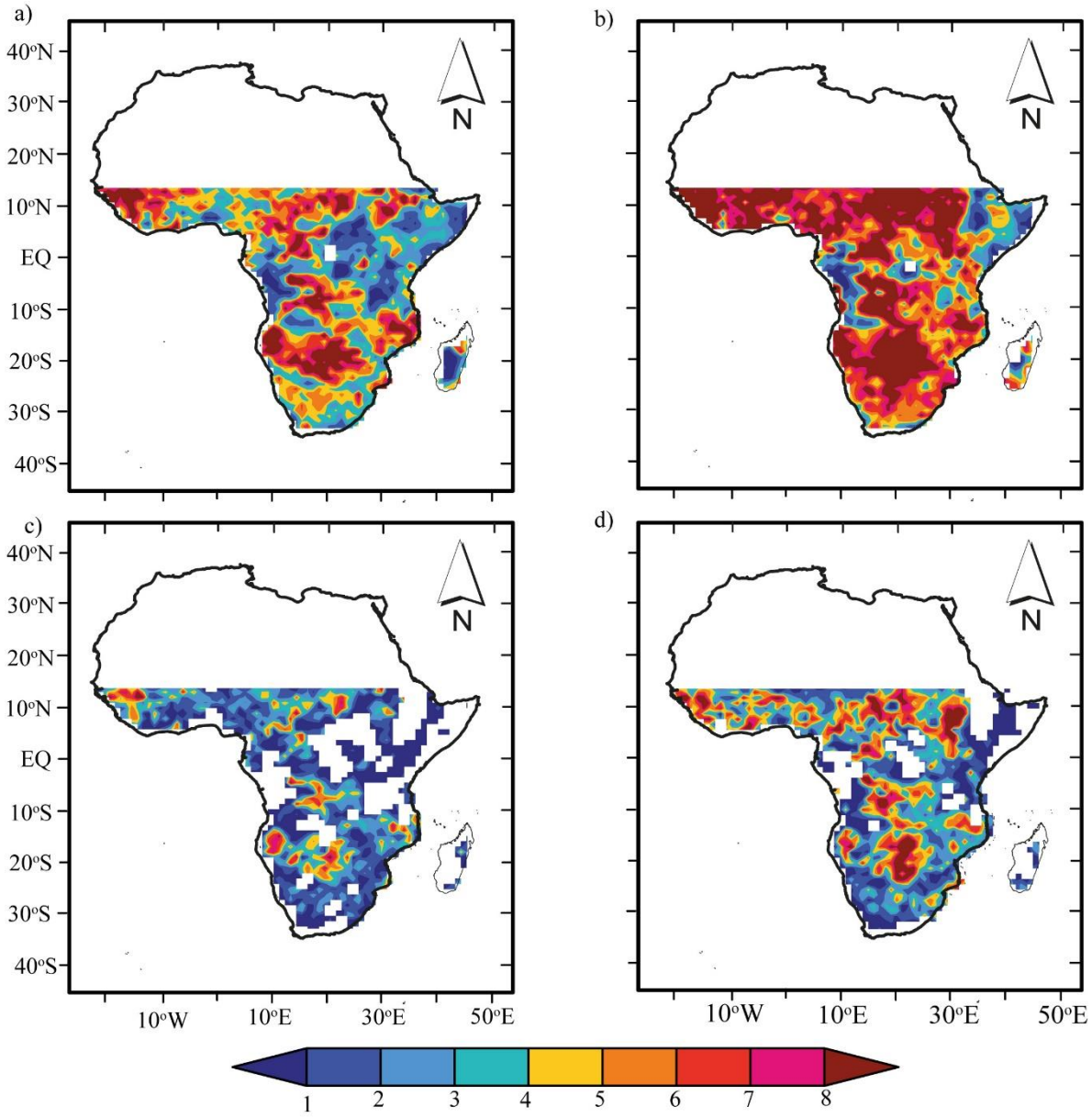

Fig. 2: Drought frequency in SSA over the period 1979-2012 for (a) $PDSI_{\_PM} < -2$ (b $PDSI_{\_TH} < -2$ (c) $PDSI_{\_PM} < -4$ (d) $PDSI_{\_TH} < -4$

Fig. 3 shows maps of the mean annual drought intensity between the moderate (top panel) and extreme drought events (bottom panel) for both scPDSI. But $scPDSI_{TH}$ show more intensification and affected larger area than in $scPDSI_{PM}$. Fig. 3a-b presents spatial intensity for moderate droughts with similar spatial pattern and magnitude as in Fig. 2a-b. The result show places with high (low) intensities but extreme droughts are more intensified in $scPDSI_{TH}$ relative to $scPDSI_{PM}$ (Fig. 2c-d).

Preprints (www.preprints.org) | NOT PEER-REVIEWED | Posted: 24 December 2020 doi:10.20944/preprints202012.0620.v1

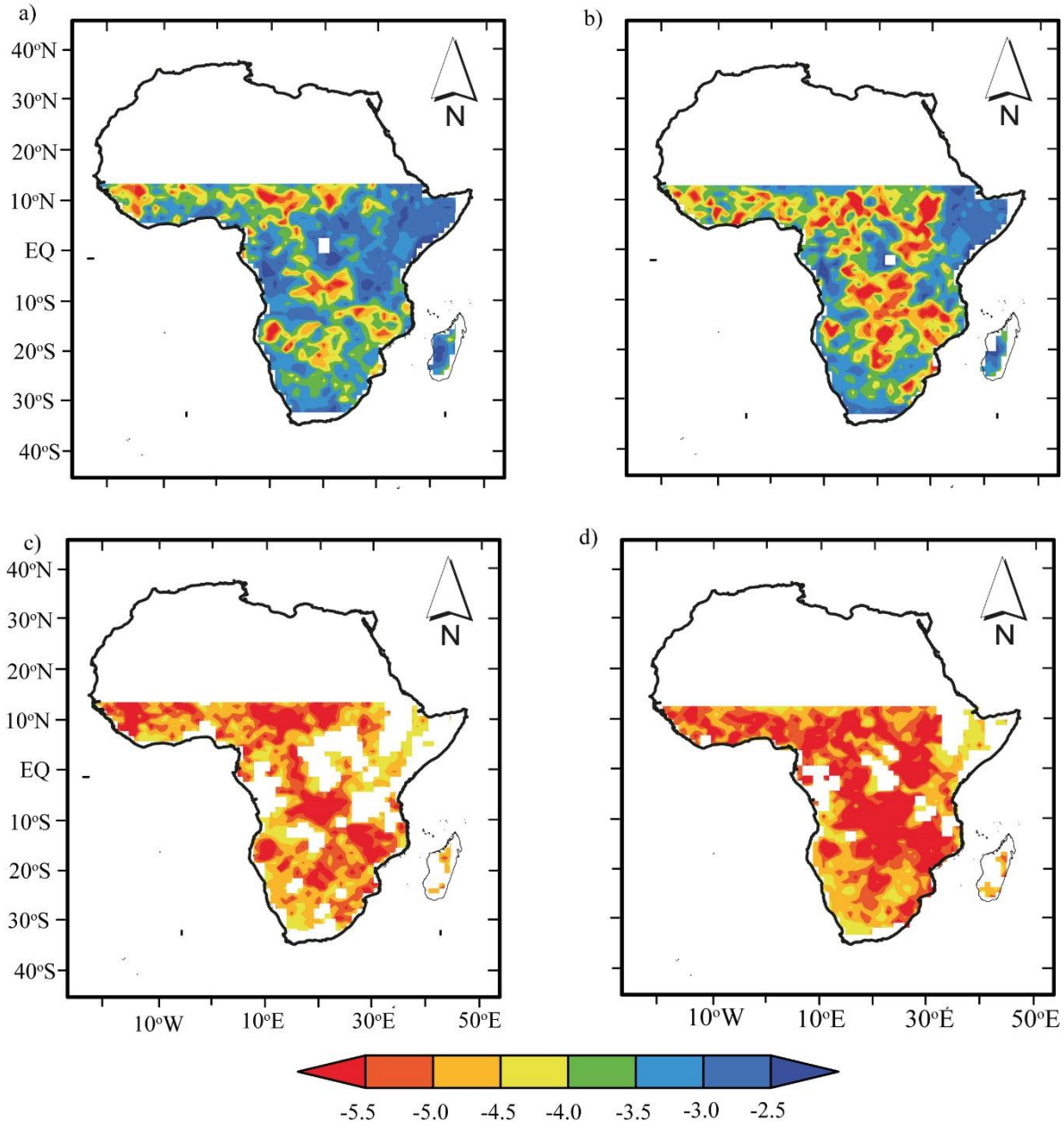

Fig. 3: Same as Fig. 2 but for Drought intensity

To understand the trend and temporal changes in drought intensities for each grid, regional trends in drought intensity for SSA and three selected regions (see Fig. 1a) were investigated and the result is shown here in Fig. 4. We observe that the interannual variations in moderate drought for both scPDSI datasets show increased trend in the whole SSA, the SSG and the southern Africa regions respectively (Fig 4a-b). In contrast, only the HoA exhibited stationarity in drought intensity but intensified over the period 1979-2012.

Preprints (www.preprints.org) | NOT PEER-REVIEWED | Posted: 24 December 2020 doi:10.20944/preprints202012.0620.v1

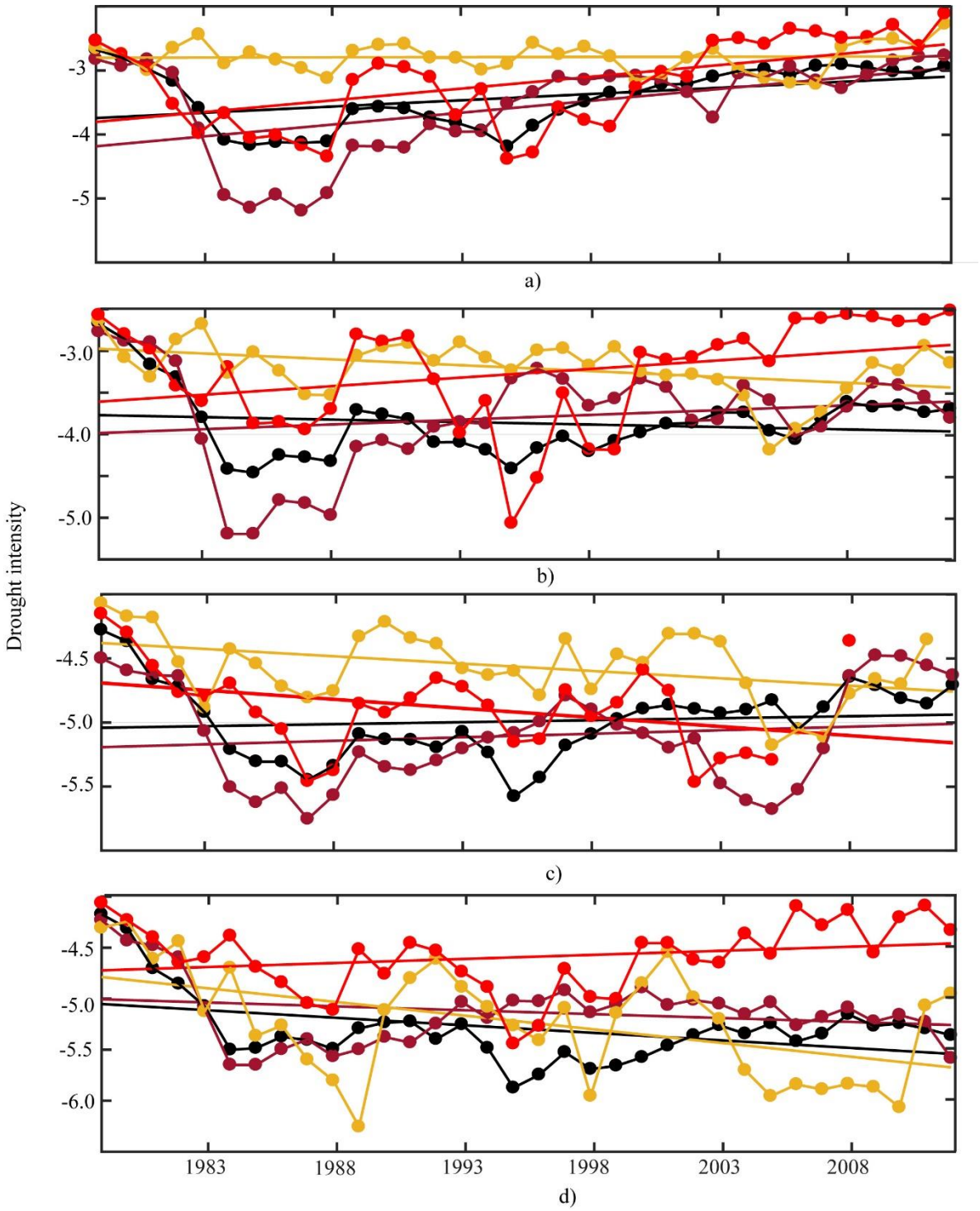

Fig. 4: Inter-annual variation of drought intensity for drought category in SSA over the period 1979-2012 for (a) scPDSI$_{_PM}$ < -2 (b) scPDSI$_{_TH}$ < -2 (c) scPDSI$_{_PM}$ < -4 (d) scPDSI$_{_TH}$ < -4. SSA (Black colour lines), Sudano-Saheliean-Guinean coast (SSG) (Brown colour lines), HoA (Gold colour lines) and Southern Africa (SAR) (Red colour lines).

Fig. 5 show the analysis of drought relationship for frequency, areal extent and intensity over SSA from 1979–2012. Fig. 5a-b shows the inter-annual variation in frequency and areas affected (shown in bar graphs) for moderate (Fig. 5a) and extreme (Fig. 5b) droughts. In all, the frequency and area affected (in km) varied considerably where more (less) frequent droughts affected larger (smaller) land area respectively (Fig. 5a-b).

 doi:10.20944/preprints202012.0620.v1

Comparatively, we observe mid-1980s, 1990s and 2000s showed significantly affected areas under moderate droughts than in extreme droughts. However, the drought affected area in scPDSI$_{PM}$ decreased after 1995 while that of scPDSI$_{TH}$ increased respectively over the period.

Next, the relationship between drought intensity and frequency was compared (Fig. 5a, d). The temporal changes in drought intensity show opposite trends relative to frequency in both datasets (Fig. 5a, d). Moderate drought shows more intensification than extreme droughts after 1995 onwards (Fig. 5c-d). However, considerable disagreement in their interannual variations both scPDSI dataset especially after 1995 was observed similar to interannual variations in frequency. Similarly, more (less) frequent droughts have low (high) intensity. Thus, our results analysis is consistent with previous regional studies where Thornthwaite method is reported to exaggerate drought frequency and intensity [8,53].

Preprints (www.preprints.org) | NOT PEER-REVIEWED | Posted: 24 December 2020 doi:10.20944/preprints202012.0620.v1

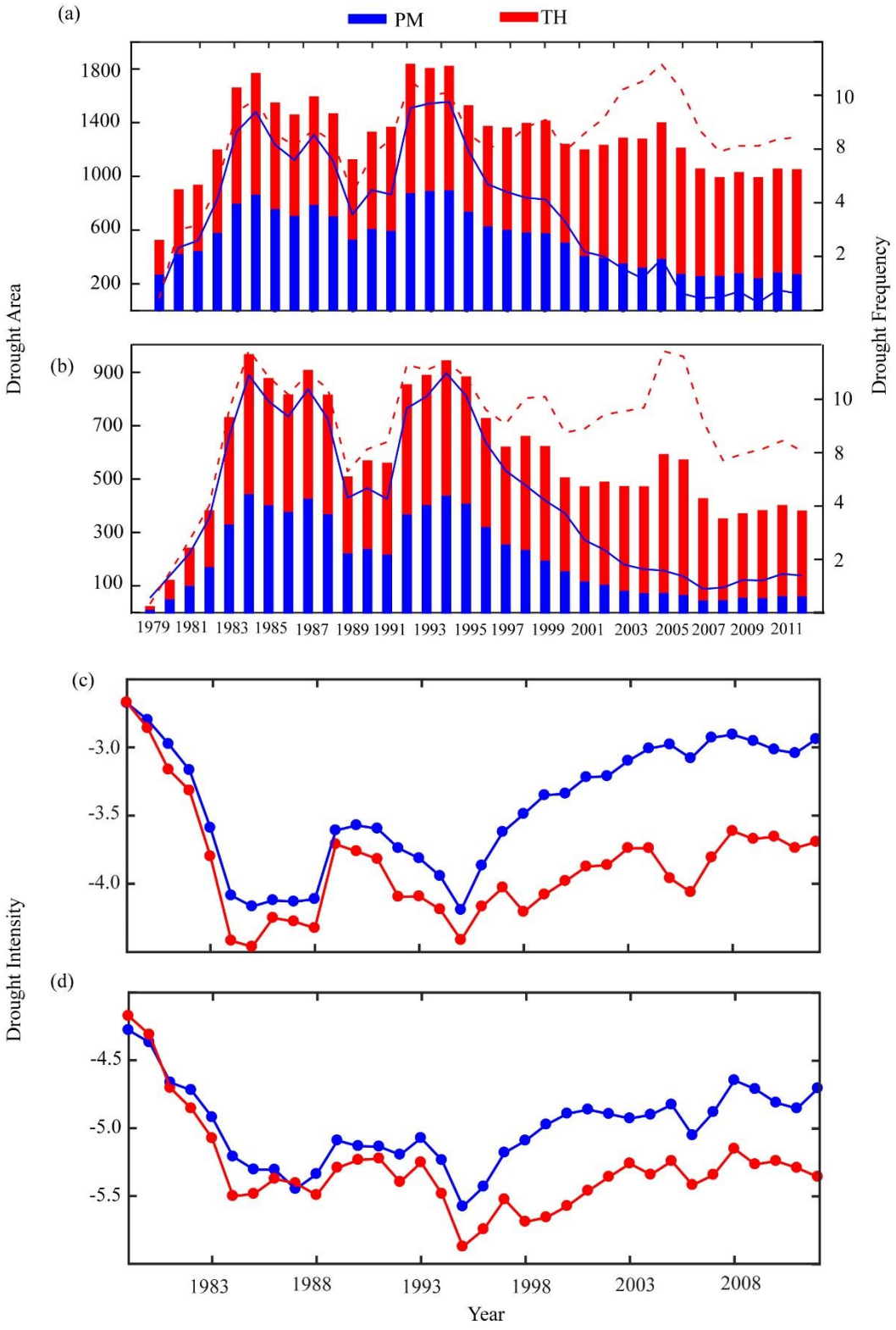

Fig 5: Drought frequency-areal extent relationship based on regional average time series in SSA. (a) Frequency-areal extent relationship for PDSI <-2 (b) Frequency-areal extent relationship for scPDSI <-4 over the period of 1979–2012 (c) The drought intensity of scPDSI <-2 (d) The drought intensity of scPDSI <-4 over the period of 1979–2012. $scPDSI_{\_PM}$ (Blue colour lines) and $scPDSI_{\_TH}$ (Red colour lines).

Preprints (www.preprints.org) | NOT PEER-REVIEWED | Posted: 24 December 2020 doi:10.20944/preprints202012.0620.v1

3.2. *Spatial-temporal trends of Wetting and Drying*

3.2.1 Spatial variations in Wetting and Drying trends

Fig. 6 shows the spatial distribution of linear trends for scPDSI$_{PM}$ and scPDSI$_{TH}$ on per-pixel basis over the period 1979-2012 estimated based on MK and Sen Slope estimator. Fig. 6a-b show trends of wet-dry variation from MK test and Fig. 6c-d shows the direction of trend by Sen Slope estimator.

In Fig 6a, we observe scPDSI$_{PM}$ showed spatially distinct wetting trend in SSG and parts of SAR (in southwest and central areas) at a rate of >0.8/10years. The HoA showed slight increasing wetting trend (< 0.4/10years) mostly in the interior of the Ethiopian highlands. Similarly, from Fig 6b, we observe scPDSI$_{TH}$ showed slight wetting trends along the SSG and parts of central and southwest of SAR (i.e. 0.4/10years).

Generally, we observe the agreement of both data to depict wetting trends in the other parts of SSA. The wetting trends in the SSG and SAR is mainly attributed to the greening and increasing P. On the other hand, drying trend dominates the southern part of HoA [i.e. 30^{o}E-52^{o}E, 0^{o}-20^{o}S] and the northern part of SAR in both scPDSI datasets. A distinct drying trends were observed (decreasing) in both scPDSI data in Fig. 6b for many areas south of HoA (at >1.2/10years). In contrast, the equatorial regions and small parts of the Congo Basin and Guinea coast showed drying (wetting) trends. The remaining areas presented no trends in scPDSI. Both datasets showed some discrepancies in capturing well the wet (dry) in few areas and we attribute the discrepancies to the choice of PET used.

Preprints (www.preprints.org) | NOT PEER-REVIEWED | Posted: 24 December 2020 doi:10.20944/preprints202012.0620.v1

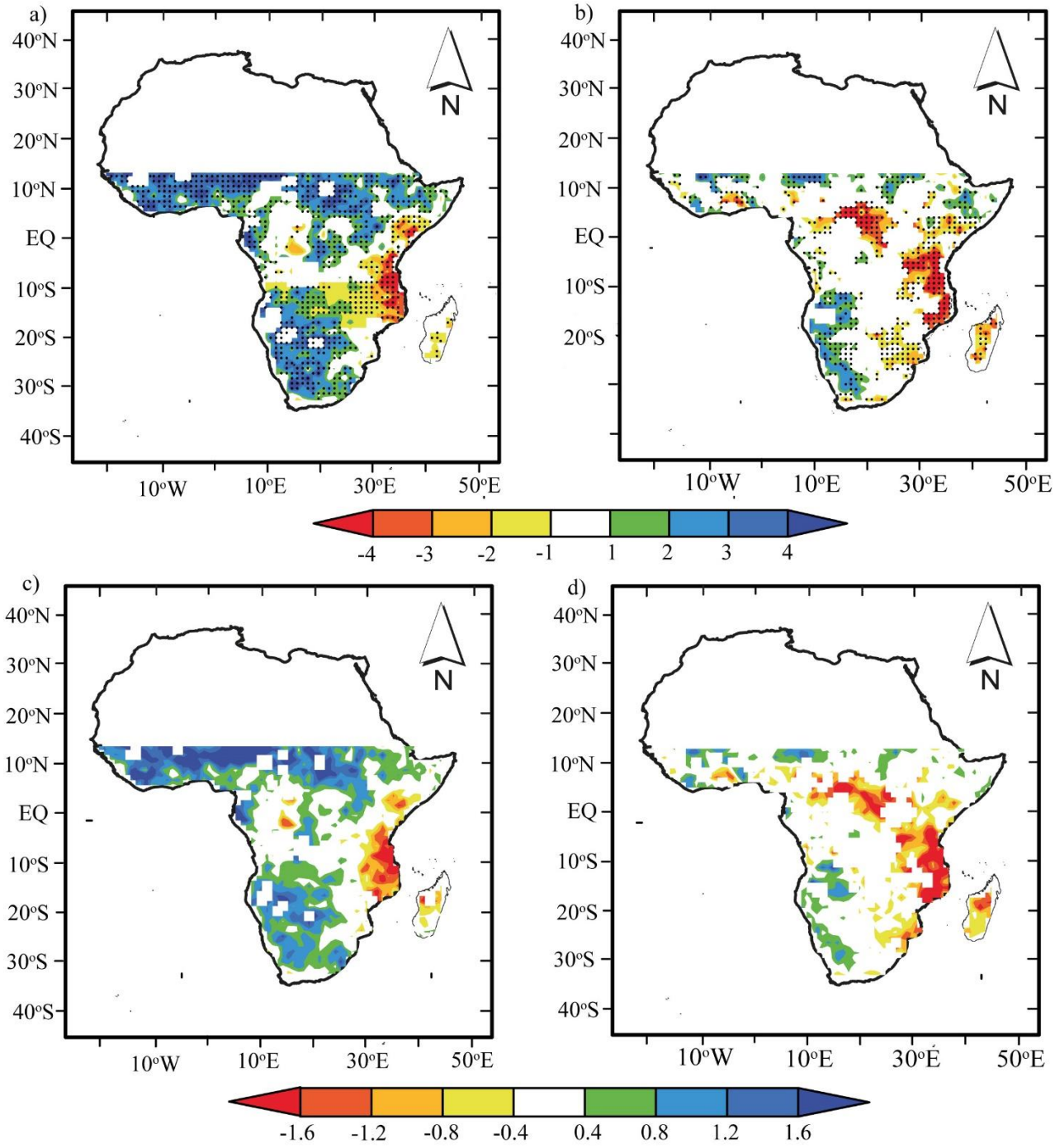

Fig. 6. Pixel-wise linear trends using the Mann Kendall and Theil–Sen slope method over the period 1979-2012 for (a) scPDSI$_{PM}$ (b) scPDSI$_{Th}$. Values are expressed in changes per decade. A positive (negative) value indicates a wetting (drying) Shading indicates where correlations are significant for the Pearson product-moment correlation (α = 0.05).

3.2.2 Temporal variations in Wetting and Drying trends

We also examined the temporal variations of regional wetting and drying conditions. We performed the linear trends using Theil–Sen slope method and the results are presented in Fig. 7. Interestingly, the interannual variations in wet and dry trends show opposite trend in both datasets after mid-1990s consistent with results in Fig. 5c-d, where similar results were observed.

Preprints (www.preprints.org) | NOT PEER-REVIEWED | Posted: 24 December 2020 doi:10.20944/preprints202012.0620.v1

In addition, we observed a widening gap between $scPDSI_{TH}$ and $scPDSI_{PM}$ after the mid-1990s in SSG and HoA, even in cases where both data show increased trend except for SAR where the gap narrow. The decline in number of weather stations, time span and quality of historical climate data over SSG and HoA as reported in [29] may explain this gap after the mid-1990s. This is because drought characteristics are sensitive to data time span and resolution [54]. Contrary to SAR with relatively more reliable climate data (Fig. 7d).

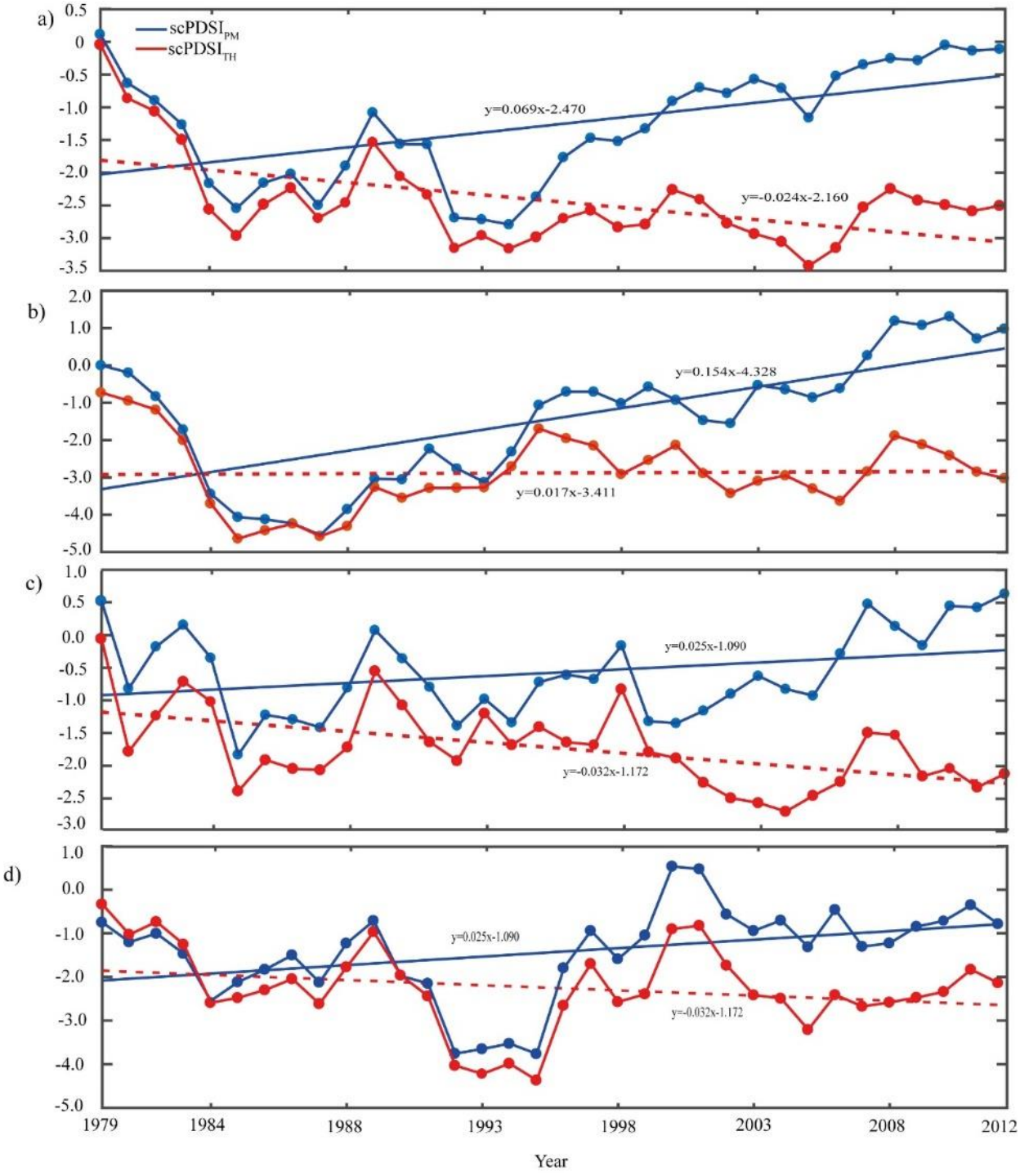

Fig. 7. Regional trends for scPDSIPM and scPDSITh in (a) Sub-Sahran Africa (SSA) (b) Sudano-Sahelian-Guinean coast (SSG) (c) Horn of Africa (HoA) (d) Southern Africa region (SAR) respectively

Preprints (www.preprints.org) | NOT PEER-REVIEWED | Posted: 24 December 2020 doi:10.20944/preprints202012.0620.v1

over the period of 1979–2012. A positive value indicates a wetting trend, and a negative value indicates a drying trend with solid (red dashed) lines

3.2.3 Temporal Variability of Remotely Sensed Precipitation and Vegetation changes

Fig.8 shows the interannual variation of P and NDVI anomalies in SSA and three regions during 1982-2012 based on regional average of P and NDVI anomalies at each grid. This analysis helps us to track dry spell and vegetation stress to understand the characteristics of scPSCI variations to response of P and NDVI. From Fig. 8, SSA P increased at a rate of 0.12mmyr^{-1} whereas SSG (at 0.036mmyr^{-1}) and SAR (0.012mmyr^{-1}) showed slight increase in P respectively. Except for HoA, increase in P corresponded to increased trend in NDVI values which means that vegetation is usually restored to a normal status after a drought ends. This result finding is consistent with wetting conditions in Fig. 3a-b for SSG and SAR and consistent with previous studies. On the other hand, NDVI trend in SAR showed a declining trend while P increased over the period 1982 to 2012. This inconsistency in Fig 9e could be due in part to changes in LUCL or explained by the 1997/1998 warm event NDVI anomalies in [55].

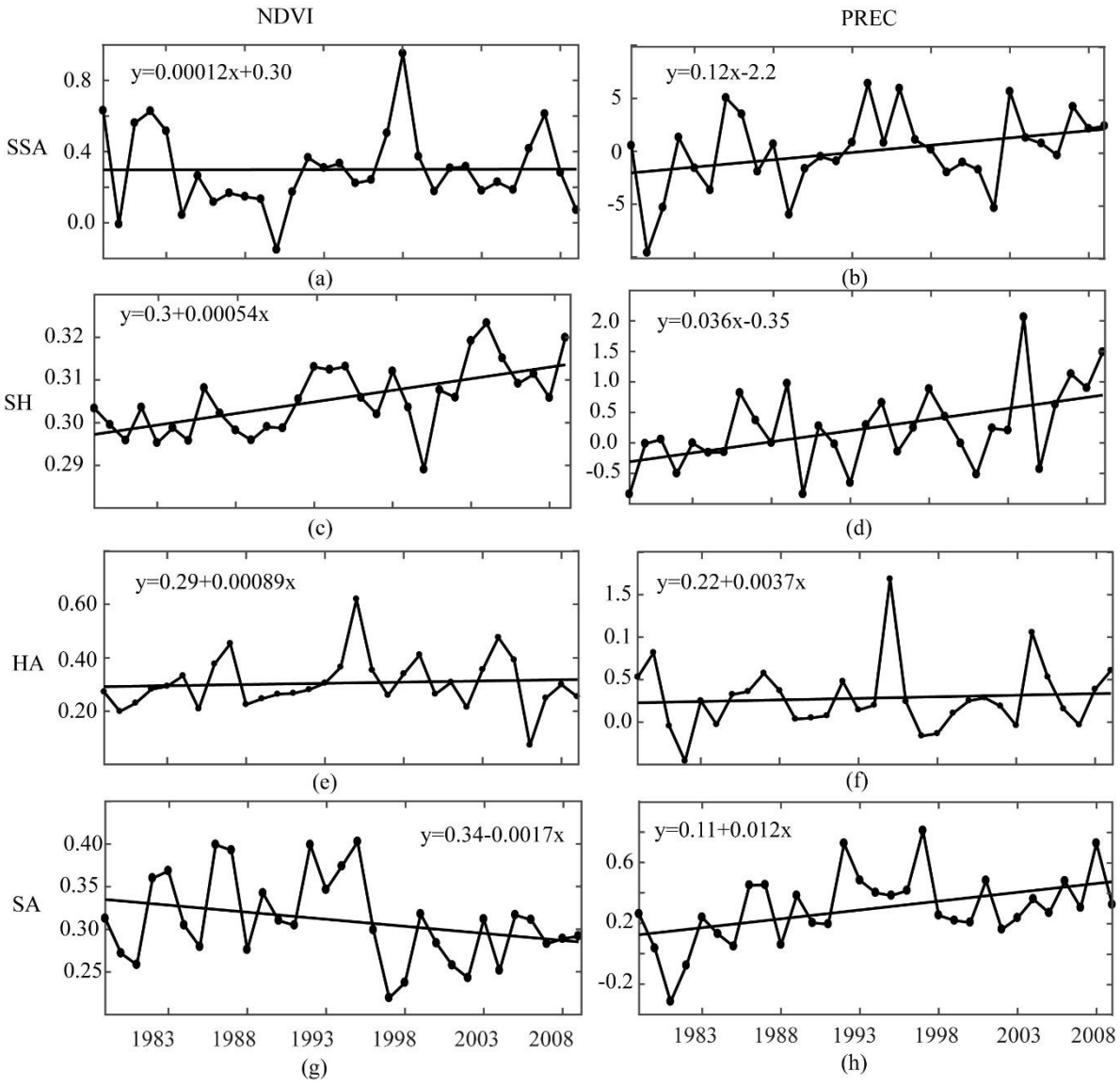

Fig. 8. Interannual variation of PRE and NDVI anomalies in SSA and three regions during 1982-2012. The solid lines indicate the linear fits during 1982-2012

Preprints (www.preprints.org) | NOT PEER-REVIEWED | Posted: 24 December 2020 doi:10.20944/preprints202012.0620.v1

3.3 *Correlation analysis of dry-wet spills and its influencing factors*

3.3.1 Influences of land surface and vegetation variables

Fig. 9 presents the spatial correlation results scPDSI with P and NDVI anomalies in SSA for the period of 1982–2012 at annual scale respectively. The correlation results show spatial patterns of pixels where shaded areas denote areas where the tests were significant at the 5% level (Fig. 9).

During the MJJASO season (see Fig. A1a-b), the NH (wet) and SH (dry) contrast show a distinct north-south pattern with P and NDVI where the wet/dry contrast appears to shift seasonally. Similarly, NDJFMA season (Fig. A1c-d), correlation patterns changed as expected with same sign and order of magnitude as above. The result is consistent with past studies that asserts that P favour's vegetation growth and that drought events may disturbs vegetation growth [29].

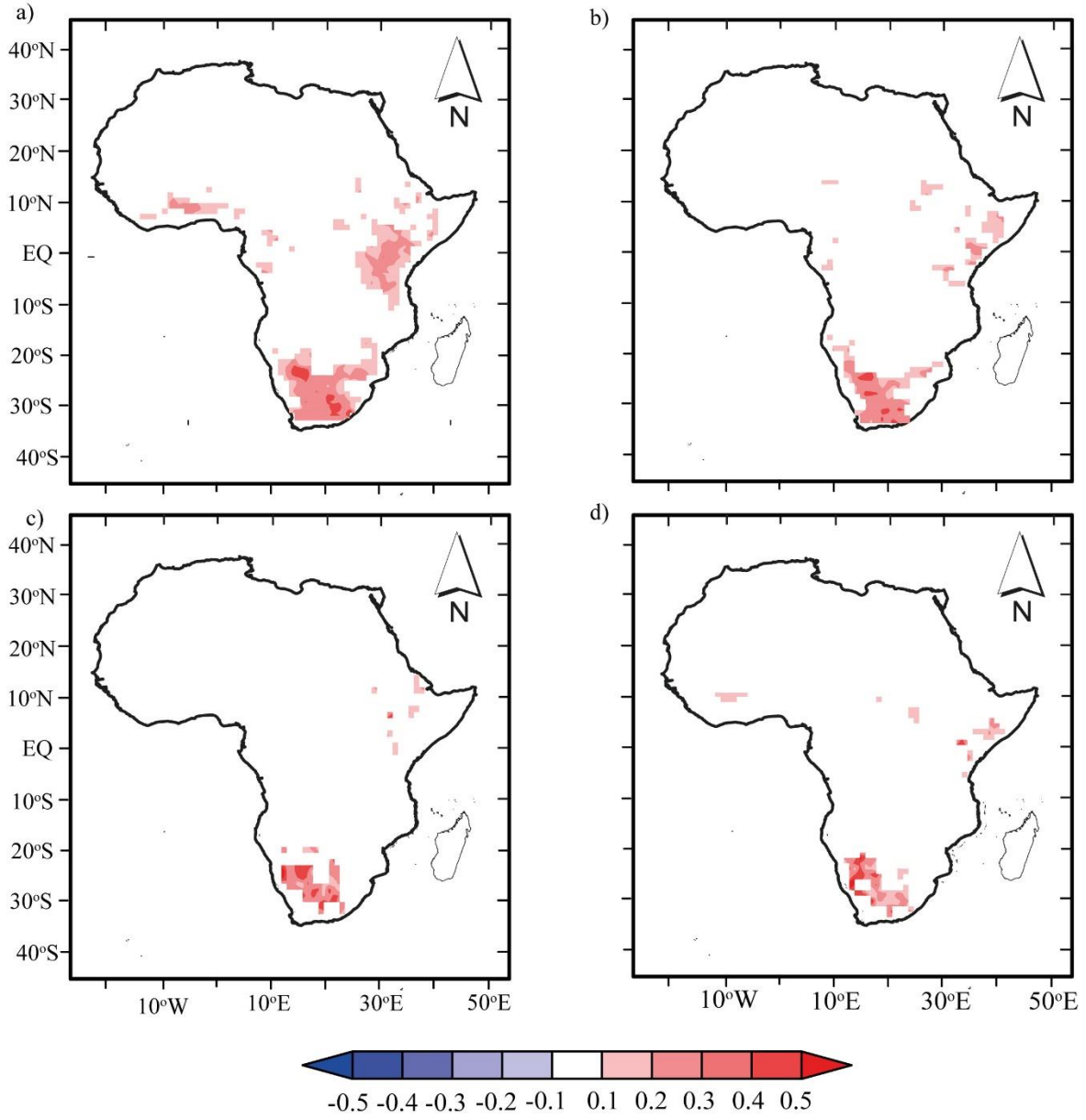

Fig. 9. Pixel-wise correlation coefficients between annual mean PDSI with the annual mean P and NDVI anomalies in SSA for period 1982–2012: (a) scPDSI$_{PM}$ and P anomaly, (b) PDSI$_{TH}$ and P anomaly (c) scPDSI$_{PM}$ and NDVI anomaly, and (d) scPDSI$_{TH}$ and NDVI anomaly. The shaded areas denote

Preprints (www.preprints.org) | NOT PEER-REVIEWED | Posted: 24 December 2020 doi:10.20944/preprints202012.0620.v1

areas where the tests were significant at the 5% level and areas that are not significant at the 5% level are masked out (white shades).

3.3.2 Influences of teleconnections

Fig. 10 show pixel-wise correlation coefficients based on annual values between spatially averaged scPDSI and circulation indices (i.e. ENSO and IOD) using simple correlational analysis to understand the temporal dynamics. Overall, on an annual scale (Fig. 10), we observe both ENSO and IOD show two phases (dipole). Fig. 10a-b show positive anomalies in SSG west tips of the Atlantic Ocean at latitudes 0°-18°S, southern tip and southeast of SAR and negative anomalies occurred at east of 5°N-15°S. In contrast, IOD in Fig. 10c-d show similar order of magnitude opposite phase to ENSO widespread weak correlation values with ENSO and IOD responses.

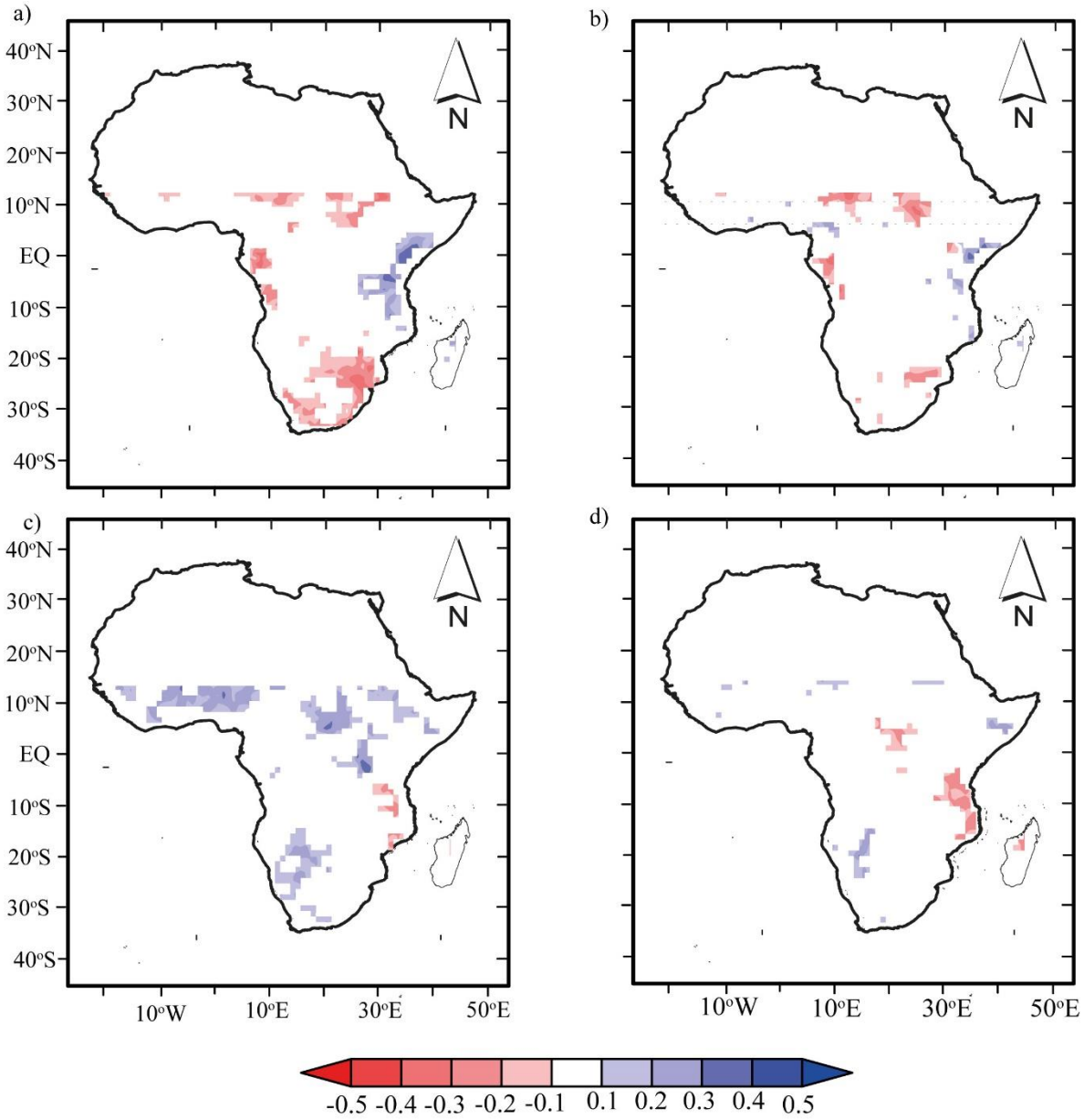

Fig. 10. Distribution of the correlation between spatial average drought indices with ENSO and IOD events. Top right panel (a) scPDSIPM and ENSO, Top left panel (b) scPDSITH and ENSO, Bottom left panel (c) scPDSIPM and IOD, bottom right panel (d) scPDSITH and IOD. The shaded areas denote

Preprints (www.preprints.org) | NOT PEER-REVIEWED | Posted: 24 December 2020 doi:10.20944/preprints202012.0620.v1

areas where the tests were significant at the 5% level and areas that are not significant at the 5% level are masked out (white shades).

4. Discussion

Generally, SSA is essentially an agrarian society, where agriculture systems depend wholly on P. Thus, any delay in P in space and time places huge demand on water availability for agricultural productions and other sectors of the society. There is enough evidence that the severe drought events in SSA over the years affected millions of people, livelihoods and the economy [2]. On the other hand, our understanding of SSA droughts characteristics, trends and the underlying mechanism is largely hampered by lack of reliable long-term climate data from weather stations.

Recent availability of specialized global drought datasets and remote sensing makes it possible to assess drought in any location across the globe. Here, we combine from multiple dataset sources to assess droughts characteristics, trends and their underlying mechanism to understand droughts evolution in SSA. Based on scPDSI data (based on Penman–Monteith and Thornthwaite methods), we assessed drought characteristics and long-term trends using Mann Kendall and Sen's slope test in SSA over the period 1979-2012. In addition, to analyse the temporal patterns and trends of land surface variables, we used the remotely sensed P and NDVI anomalies based on the MK and Sen's slope test. Also, drought events link to land surface variables, vegetation changes and climate circulations (i.e. ENSO and IOD) were investigated using simple correlational analysis to understand the factors that drives these drought changes in the region.

In our first analysis, we assessed drought characteristics in terms of the frequency, intensity and affected area based on annual mean scPDSI$_{PM}$ and the scPDSI$_{TH}$ across SSA over period of 1979-2012. Two fixed thresholds (i.e. scPDSI <-2 (-4)) were used to denote moderate (extreme) droughts respectively. These thresholds have been widely adopted and used in many studies [6, 8, 9, 12].

Our results showed that the two scPDSI data differed in their representation of drought characteristics across SSA. The spatial analysis (Fig. 3 and 4) highlights moderate and extreme droughts similarity in capturing drought frequency (intensity) in the northwest tips of the SHG, patches north and south of the Congo basin and patches 18^{o}S-22^{o}S (of the Kalahari Desert to the southeast tip of Mozambique). In contrast, disagreements in the datasets were observed in few areas in SSA that are characterized by complex topography, large water bodies/wetlands and dense vegetation were captured in both scPDSI datasets.

Moderate droughts occurred more frequently than extreme drought (in Fig. 3). However, scPDSI$_{TH}$ occurred more frequently and affected larger areas relative to scPDSI$_{PM}$ (Fig. 3a-d). This results finding is consistent with previous studies where scPDSI$_{TH}$ exaggerates drought intensification (as it responds only to changes in T) relative to scPDSI$_{PM}$ (which is constrained by the inclusion of many climate variables). Similar reasons are assigned Fig 4 but for intensity. We further investigated the trends in drought intensities for each grid. Here, we focused on the regional trend in drought intensities over the whole SSA and three selected regions (see Fig. 5a-b). Results showed increased trend in SSA, SSG and SAR except for HoA which showed stationarity in drought intensity over the period 1979-2012.

The relationship between drought frequency and areal coverage was investigated. Fig. 6a-b shows the inter-annual variation in frequency (shown as line graph) and affected areas (shown as bar graphs) under moderate and extreme droughts. The frequency and area affected by droughts varied

Preprints (www.preprints.org) | NOT PEER-REVIEWED | Posted: 24 December 2020 doi:10.20944/preprints202012.0620.v1

considerably (Fig. 5a-b). This result was also reflected in Fig 6c with the temporal changes in drought intensity but opposite trend. This relation is expected as drought intensity is related to the frequencies of occurrence. On the other hand, considerable disagreement is shown after 1995 where both dataset estimates affected areas differently. scPDSI$_{PM}$ followed an opposite trend relative to scPDSI$_{TH}$ is consistent with previous regional studies where Thornthwaite method exaggerates drought frequency and intensity and hence drought affected area [8,53].

We analysed the trend of wet-dry variation over the period 1979-2012 for both datasets. The results findings showed varying magnitudes and trend values for the region. The spatially distinct wetting trend in Fig 7a-b is consistent with the greening and increasing P in parts of the SSA consistent as shown in previous studies [9]. On the other hand, some discrepancies observed in both datasets in capturing the wet (dry) spells may be attributed to the choice of PET consistent with past studies [9,16].

Furthermore, we investigated the trends of remotely sensed climate variables and vegetation changes to understand scPSCI variability to response of P and NDVI. We performed regional average of P and NDVI anomalies for the whole SSA at each grid point to track dry spell and vegetation stress. Here, we used time span of 1982-2012 of satellite data of P and NDVI products to assess the interannual variation of P and NDVI anomalies in SSA and three selected regions (see Fig. 9).

Generally, there appears to be a high degree of similarity between the trends of P and NDVI in estimating wet and dry spells (in Fig. 9) with Fig 8 (from both scPDSI data). Increased P anomalies over SSA (at a rate of 0.12mmyr^{-1}), SSG (at 0.036mmyr^{-1}), SAR (0.012mmyr^{-1}) and HoA (0.012mmyr^{-1}) is consistent with wetting conditions as shown in previous studies about P leveling over the region [14, 18].

On the other hand, increased in P anomalies corresponded to increased interannual variability in NDVI values which means that vegetation is usually restored to a normal status after a dry spell ends except for HoA where NDVI variability in SAR showed a declined trend while P increased over the period 1982 to 2012. This inconsistency in Fig 9e could be due in part to changes in LUCL or explained by the 1997/1998 warm event NDVI anomalies in [55].

In order to explain the SSA characteristics of dry-wet variation, we conducted correlation analysis to understand the relationship between scPDSI with climatic, vegetation and atmospheric processes. The correlation results show spatial pattern of pixels over the period 1982-2012 (annual scale in Fig. 9 and seasonal scale in Fig. A1 and 2. Generally, positive correlation between P (NDVI) anomalies and PDSI is widespread across HoA, SAR and patches of SSG especially along the guinea coast at annual and seasonal scales. A seasonal shift from NH and SH where observed for monsoon P anomalies response to PDSI (Fig. A1). We found that MJJASO (Fig. A1a-b) sensitivities were evident largely in SSG while that of NDJFMA (Fig. A1c-d) is evident in SAR and HoA. Similarly, in Fig. A2, the NDVI anomalies relation with PDSI is consistent with that of P anomalies but at varying magnitude in space. This result finding is consistent with both annual and seasonal climatology of P and NDVI and underscores these two variables as major influencing variables to extreme events in SSA.

Last but not least, previous studies have attempted to link droughts episodes to climate circulations (see [56] in the case of USA). In SSA, both Sheffield [20] and Katchele [19] mentioned that the studying the links of droughts and teleconnections is useful and intuitive. We performed pixel-wise correlation to understand the temporal dynamics (Fig. 11). The result showed that ENSO and

IOD have a significant impact on wet and dry spells and their geographical impact is consistent with that of P and NDVI anomalies. Despite the weak correlation values, this result agrees with similar studies linking droughts episodes to ENSO and IOD in Africa [28,29]. A negative (positive) correlation is associated with strong La Niña (El Niño) events, enhancing (reducing) P and hence wet (dry) spells. Similarly, IOD as a coupled ocean-atmosphere mode, indicates a negative (positive) phase described by cool (warm) SSTs, impacts droughts episodes in places consistent with ENSO but in opposite phase (Fig. 11c-d, bottom panel).

5 Conclusion

This work assessed the impact of different PET methods (i.e. scPDSI$_{PM}$ and scPDSI$_{TH}$ methods) on long-term drought trends and uses remotely sensed P and vegetation change plus observed climate circulation indices (i.e. ENSO and IOD) to investigate how these variables respond to droughts occurrences across SSA. Compared to previous regional droughts assessment in SSA, this study summarises noteworthy novelties as follows;

1. The spatial analysis of scPDSI$_{TH}$ and scPDSI$_{PM}$ differed in their representation of drought characteristics i.e. frequency, affected area and intensity) across SSA. From the droughts characteristics results, the interannual variations in moderate droughts showed a decreasing trend, and then an abrupt change after mid-1990s to present an increasing trend. We found similar results this for the data of extreme droughts.
2. Both scPDSI data showed significant drying trends in drought intensity and increasing trend in the affected areas. However, the Thornthwaite method exaggerated drought relative to the Penman–Monteith method in the warming climate.
3. Generally, increased wet spells found in transition and dry climatic region across SSA is due to increased P. The wet and dry trend results revealed consistent and significant trends in both datasets over SSA where downward trend (1979-1995) indicates increased intensity and upward trend (1995-2012) suggest decrease intensity. This results findings suggest the trends of floods (droughts) events has become more frequent in recent times under recent global warming scenarios.
4. A general pattern of negative correlation between P anomalies with PDSI occurs across SSA with the strongest relationships in locations along SSG, HoA and SAR. Positive correlation of NDVI anomalies and PDSI across SSA tend to be in small patches with modest exceptions during monsoon season and post-monsoon season in SSG, HoA and SAR. In addition, PDSI is impacted by ENSO and IOD with similar overlap in geographic distributions.

Author Contributions: Conceptualization, I.K.N. and G.W.; Data curation, I.K.N. G.W and J.L; Methodology, I.K.N. G. W, D.F.T.H and JL; Resources, G.W.; Supervision, G.W, and D.F.T.H; Validation, D.F.T.H, W.U and L.S; Visualization, A.S.B., X.S., D.L. and Z.C.; Writing–original draft, I.K.N.; Writing–review & editing, G.W, D.F.T.H, N.A.P and S.O.Y.A.

Funding: This research was funded by National Key Research and Development Program of China (2017YFA0603701), the National Natural Science Foundation of China (41875094), the Sino-German Cooperation Group Project (GZ1447).

Acknowledgments: We extend our special gratitude to the developers, managers and funding agencies of Terrestrial Hydrology Research Group (Princeton University), Climate Hazards Group (CHIRPS), ECMWF (ERA-5), GIMMS group (NDVI data), ESACCI group (LULC map), NASA-SRTM

Preprints (www.preprints.org) | NOT PEER-REVIEWED | Posted: 24 December 2020 doi:10.20944/preprints202012.0620.v1

group (DEM), and Climate Prediction Center (ENSO, IOD data) for granting access to these essential datasets in accordance to their specific data use and citation policies.

Conflicts of Interest: The authors declare no conflict of interest.

Appendix A

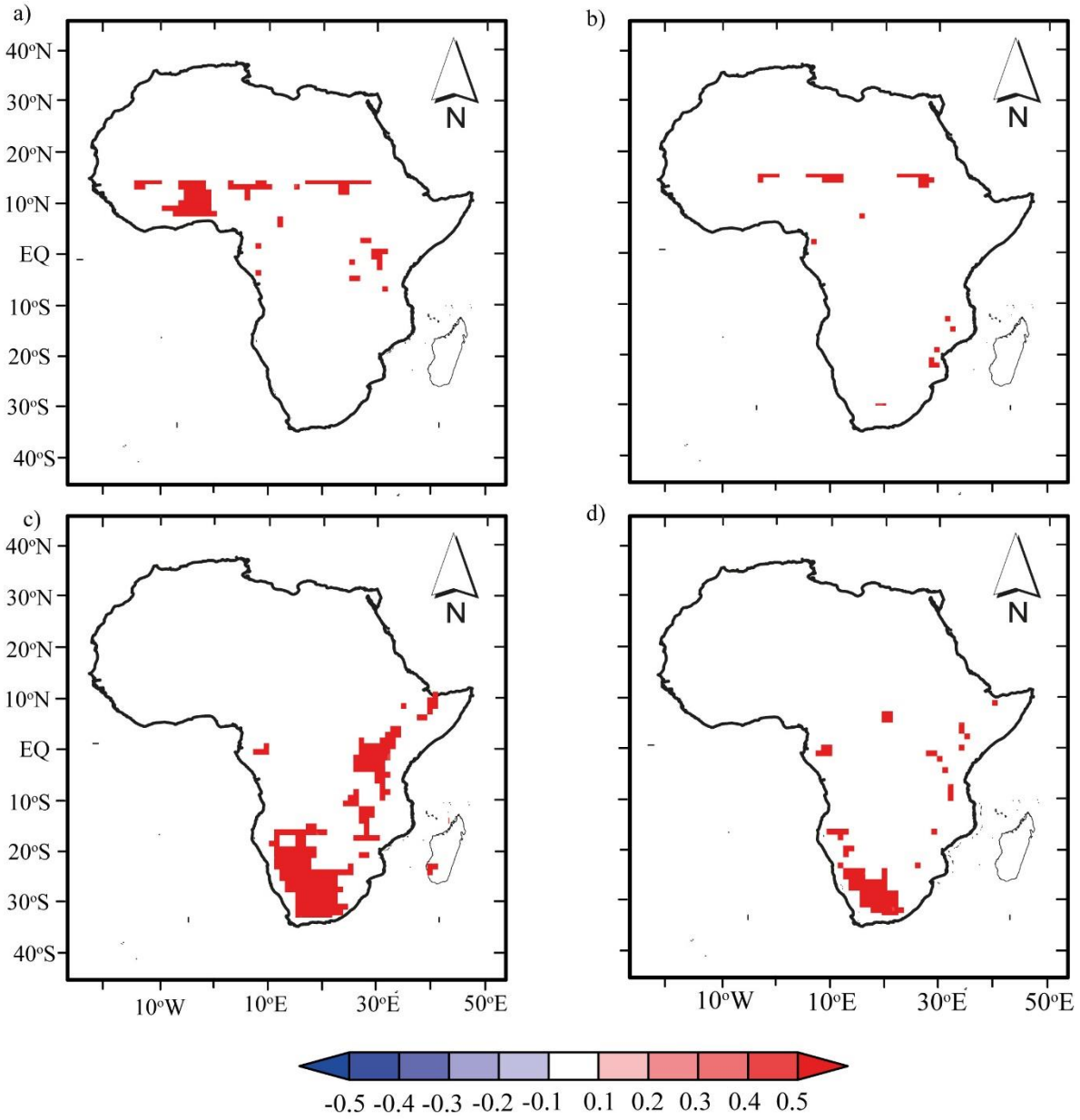

Fig. A1. Pixel-wise correlation coefficients between seasonal mean scPDSI with the seasonal mean P anomalies in SSA for period 1982–2012: (a) MJJASO scPDSI$_{PM}$ and P anomaly, (b) MJJASO PDSI$_{TH}$ and P anomaly (c) NDJFMA scPDSI$_{PM}$ and P anomaly, and (d) NDJFMA scPDSI$_{TH}$ and P anomaly. The shaded areas denote areas where the tests were significant at the 5% level and areas that are not significant at the 5% level are masked out (white shades).

Preprints (www.preprints.org) | NOT PEER-REVIEWED | Posted: 24 December 2020 doi:10.20944/preprints202012.0620.v1

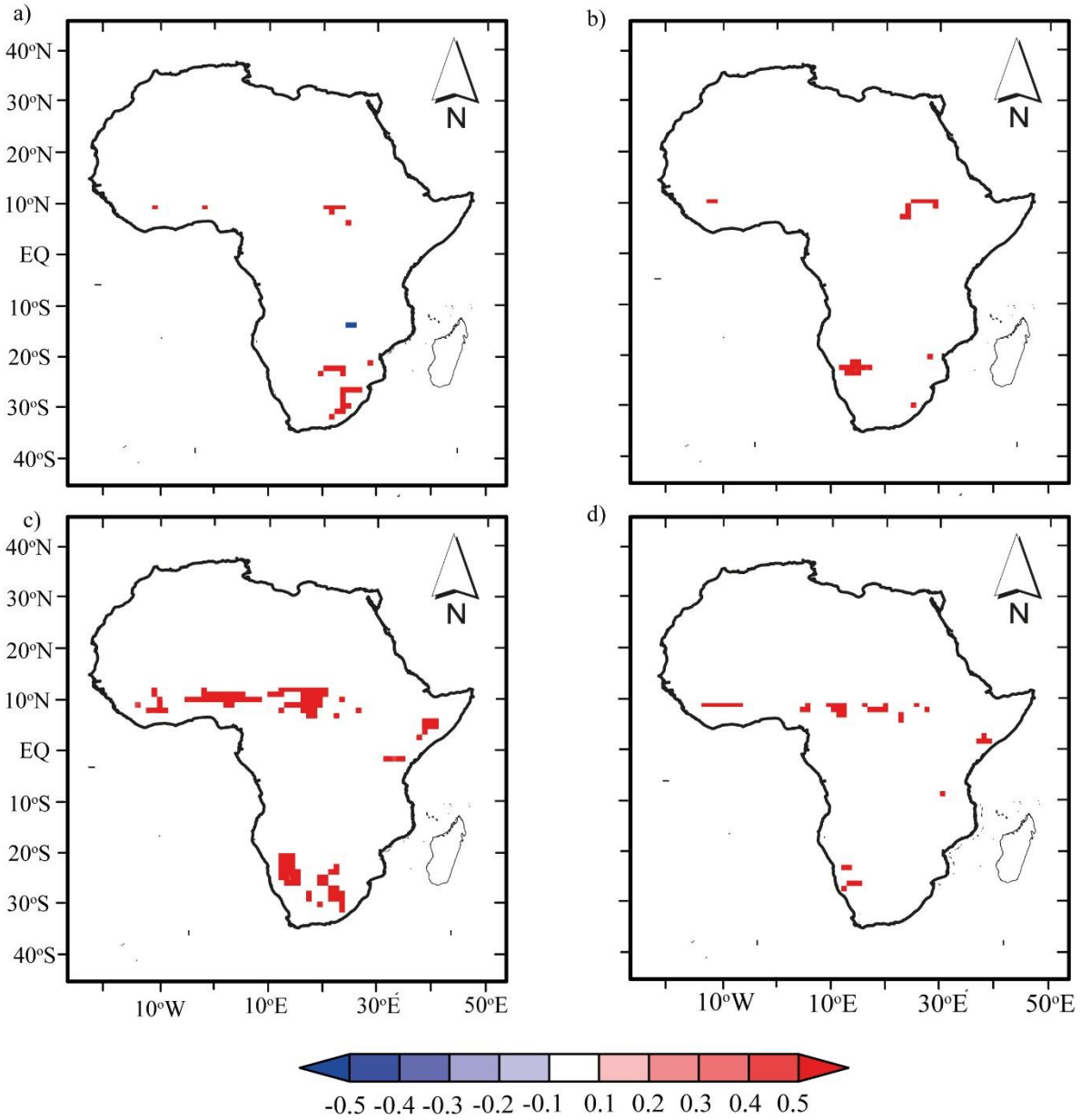

Fig. A2. Same as Fig. A1 but for NDVI

References

1. IPCC. Climate change 2014: Impacts, adaptation, and vulnerability. rep., T., Ed. Cambridge University Press, : Cambridge, United Kingdom and New York, NY, USA, 2014.
2. Guha-Sapir, D.; Below, R.; Hoyois, P. Emem-dat: The international disaster database. (6 January),
3. Bachmair, S.; Svensson, C.; Hannaford, J.; Barker, L.J.; Stahl, K. A quantitative analysis to objectively appraise drought indicators and model drought impacts. *Hydrol. Earth Syst. Sci.* **2016**, *20*, 2589-2609.
4. Bachmair, S.; Tanguy, M.; Hannaford, J.; Stahl, K. How well do meteorological indicators represent agricultural and forest drought across europe? *Environmental Research Letters* **2018**, *13*, 034042.
5. Paulo, A.A.; Rosa, R.D.; Pereira, L.S. Climate trends and behaviour of drought indices based on precipitation and evapotranspiration in portugal. *Nat. Hazards Earth Syst. Sci.* **2012**, *12*, 1481-1491.
6. Vicente-Serrano, S.M.; Beguería, S.; Lorenzo-Lacruz, J.; Camarero, J.J.; López-Moreno, J.I.; Azorin-Molina, C.; Revuelto, J.; Morán-Tejeda, E.; Sanchez-Lorenzo, A. Performance of drought indices for ecological, agricultural, and hydrological applications. *Earth Interactions* **2012**, *16*, 1-27.

7. Mishra, A.K.; Singh, V.P. A review of drought concepts. *Journal of Hydrology* **2010**, *391*, 202-216.
8. Dai, A. Increasing drought under global warming in observations and models. *Nature Climate Change* **2013**, *3*, 52-58.
9. Sheffield, J.; Wood, E.F.; Roderick, M.L. Little change in global drought over the past 60 years. *Nature* **2012**, *491*, 435-438.
10. Seneviratne, S.I. Historical drought trends revisited. *Nature* **2012**, *491*, 338-339.
11. Trenberth, K.E.; Dai, A.; van der Schrier, G.; Jones, P.D.; Barichivich, J.; Briffa, K.R.; Sheffield, J. Global warming and changes in drought. *Nature Climate Change* **2014**, *4*, 17-22.
12. Dai, A.; Trenberth, K.E.; Qian, T. A global dataset of palmer drought severity index for 1870–2002: Relationship with soil moisture and effects of surface warming. *Journal of Hydrometeorology* **2004**, *5*, 1117-1130.
13. Chen, T.; van der Werf, G.R.; de Jeu, R.A.M.; Wang, G.; Dolman, A.J. A global analysis of the impact of drought on net primary productivity. *Hydrology and Earth System Sciences* **2013**, *17*, 3885 - 3894.
14. Chen, T.; Zhang, H.; Chen, X.; Hagan, D.F.; Wang, G.; Gao, Z.; Shi, T. Robust drying and wetting trends found in regions over china based on köppen climate classifications. *Journal of Geophysical Research: Atmospheres* **2017**, *122*, 4228-4237.
15. Jr., R.R.H. A review of twentieth-century drought indices used in the united states. *Bulletin of the American Meteorological Society* **2002**, *83*, 1149-1166.
16. Wang, G.; Gong, T.; Lu, J.; Lou, D.; Hagan, D.F.T.; Chen, T. On the long-term changes of drought over china (1948–2012) from different methods of potential evapotranspiration estimations. *International Journal of Climatology* **2018**, *38*, 2954-2966.
17. Sun, Q.; Miao, C.; Duan, Q.; Ashouri, H.; Sorooshian, S.; Hsu, K.-L. A review of global precipitation data sets: Data sources, estimation, and intercomparisons. *Reviews of Geophysics* **2018**, *56*, 79-107.
18. Sun, B.; Gao, Z.; Li, Z.; Wang, H.; Li, X.; Wang, B.; Wu, J. Dynamic and dry/wet variation of climate in the potential extent of desertification in china during 1981–2010. *Environmental Earth Sciences* **2015**, *73*, 3717-3729.
19. Faustin Katchele, O.; Ma, Z.-G.; Yang, Q.; Batebana, K. Comparison of trends and frequencies of drought in central north china and sub-saharan africa from 1901 to 2010. *Atmospheric and Oceanic Science Letters* **2017**, *10*, 418-426.
20. Sheffield, J.; Wood, E.F.; Chaney, N.; Guan, K.; Sadri, S.; Yuan, X.; Olang, L.; Amani, A.; Ali, A.; Demuth, S., *et al.* A drought monitoring and forecasting system for sub-sahara african water resources and food security. *Bulletin of the American Meteorological Society* **2014**, *95*, 861-882.
21. FAO. The state of food and agriculture 2016. Food and Agriculture of the United Nations: Rome, 2016; p 196.
22. Van Loon, A.F. Hydrological drought explained. *WIREs Water* **2015**, *2*, 359-392.
23. Schellekens, J.; Dutra, E.; Martínez-de la Torre, A.; Balsamo, G.; van Dijk, A.; Sperna Weiland, F.; Minvielle, M.; Calvet, J.C.; Decharme, B.; Eisner, S., *et al.* A global water resources ensemble of hydrological models: The earth2observe tier-1 dataset. *Earth Syst. Sci. Data* **2017**, *9*, 389-413.
24. Beck, H.E.; Zimmermann, N.E.; McVicar, T.R.; Vergopolan, N.; Berg, A.; Wood, E.F. Present and future köppen-geiger climate classification maps at 1-km resolution. *Scientific Data* **2018**, *5*, 180214.
25. ESACCI. European space agency climate change initiative (esacci) land use land cover (lulc) map https://www.esa-landcover-cci.org/ (10 November),

26. Camberlin, P.; Philippon, N. The east african march–may rainy season: Associated atmospheric dynamics and predictability over the 1968–97 period. *Journal of Climate* **2002**, *15*, 1002-1019.
27. (SRTM), N.A.a.S.A.N.S.R.T.M. Home page. https://lpdaac.usgs.gov/products/srtmgl1v003/ (10 November),
28. Poccard, I.; Janicot, S.; Camberlin, P. Comparison of rainfall structures between ncep/ncar reanalyses and observed data over tropical africa. *Climate Dynamics* **2000**, *16*, 897-915.
29. Philippon, N.; Martiny, N.; Camberlin, P.; Hoffman, M.T.; Gond, V. Timing and patterns of the enso signal in africa over the last 30 years: Insights from normalized difference vegetation index data. *Journal of Climate* **2014**, *27*, 2509-2532.
30. Terrestrial Hydrology Research Group. A global dataset of palmer drought severity index (pdsi) and potential evporation (pe) at 1.0-degree, monthly resolution. http://hydrology.princeton.edu/data/pdsi/updates_1948-2012/.
31. Sheffield, J.; Goteti, G.; Wood, E.F. Development of a 50-year high-resolution global dataset of meteorological forcings for land surface modeling. *Journal of Climate* **2006**, *19*, 3088-3111.
32. Tucker, C.J.; Pinzon, J.E.; Brown, M.E.; Slayback, D.A.; Pak, E.W.; Mahoney, R.; Vermote, E.F.; El Saleous, N. An extended avhrr 8-km ndvi dataset compatible with modis and spot vegetation ndvi data. *International Journal of Remote Sensing* **2005**, *26*, 4485-4498.
33. Martiny, N.; Camberlin, P.; Richard, Y.; Philippon, N. Compared regimes of ndvi and rainfall in semi-arid regions of africa. *International Journal of Remote Sensing* **2006**, *27*, 5201-5223.
34. Funk, C.; Peterson, P.; Landsfeld, M.; Pedreros, D.; Verdin, J.; Shukla, S.; Husak, G.; Rowland, J.; Harrison, L.; Hoell, A., *et al.* The climate hazards infrared precipitation with stations—a new environmental record for monitoring extremes. *Scientific Data* **2015**, *2*, 150066.
35. IRI/LDE. International research institute climate data library. https://iri.columbia.edu/topics/data-library/ (10 November),
36. Funk, C.C.; Peterson, P.J.; Landsfeld, M.F.; Pedreros, D.H.; Verdin, J.P.; Rowland, J.D.; Romero, B.E.; Husak, G.J.; Michaelsen, J.C.; Verdin, A.P. A quasi-global precipitation time series for drought monitoring. Series, G.S.D., Ed. US, 2014; p 4.
37. Agutu, N.O.; Awange, J.L.; Zerihun, A.; Ndehedehe, C.E.; Kuhn, M.; Fukuda, Y. Assessing multi-satellite remote sensing, reanalysis, and land surface models' products in characterizing agricultural drought in east africa. *Remote Sensing of Environment* **2017**, *194*, 287-302.
38. Ullah, W.; Wang, G.; Ali, G.; Tawia Hagan, D.F.; Bhatti, A.S.; Lou, D. Comparing multiple precipitation products against in-situ observations over different climate regions of pakistan. *Remote Sensing* **2019**, *11*, 628.
39. (ECMWF), E.C.f.M.-R.W.F. Home page. http://apps.ecmwf.int/datasets/data/interim-full-daily/levtype=sfc/
40. Climate Prediction Center (CPC) of the National Weather Service, U.S.w. Http://www.Cpc.Ncep.Noaa.Gov. http://www.cgd.ucar.edu/cas/catalog/climind/IOD.signal.annstd.ascii
41. database, C.P.C. http://www.cpc.ncep.noaa.gov/data/indices/
42. Smith, T.M.; Reynolds, R.W.; Peterson, T.C.; Lawrimore, J. Improvements to noaa's historical merged land–ocean surface temperature analysis (1880–2006). *Journal of Climate* **2008**, *21*, 2283-2296.
43. Palmer, W. *Meteorological drought*. US Weather Bureau: Washington, DC, 1965.
44. ESRI. Arcgis® 10.3.1 software www.esri.com (10 November),

45. Microsoft Inc. Microsoft inc home page. https://www.microsoft.com/en-us/ (10 November),
46. Shlien, S. Geometric correction, registration, and resampling of landsat imagery. *Canadian Journal of Remote Sensing* **1979**, *5*, 74-89.
47. Nooni, I.K.; Duker, A.A.; Van Duren, I.; Addae-Wireko, L.; Osei Jnr, E.M. Support vector machine to map oil palm in a heterogeneous environment. *International Journal of Remote Sensing* **2014**, *35*, 4778-4794.
48. software, M.l. Home page. https://ww2.mathworks.cn/products/matlab.html
49. Mann, H.B. Nonparametric tests against trend. *Econometrica* **1945**, *13*, 245-259.
50. Kendall, M.G. *Rank correlation methods.* Charles Griffin: London, 1975.
51. Sen, P.K. Estimates of the regression coefficient based on kendall's tau. *Journal of the American Statistical Association* **1968**, *63*, 1379-1389.
52. Nooni, I.K.; Wang, G.; Hagan, D.F.T.; Lu, J.; Ullah, W.; Li, S. Evapotranspiration and its components in the nile river basin based on long-term satellite assimilation product. *Water* **2019**, *11*, 1400.
53. Zhai, J.; Su, B.; Krysanova, V.; Vetter, T.; Gao, C.; Jiang, T. Spatial variation and trends in pdsi and spi indices and their relation to streamflow in 10 large regions of china. *Journal of Climate* **2010**, *23*, 649-663.
54. Golian, S.; Javadian M.; Behrangi, A. On the use of satellite, gauge, and reanalysis precipitation products for drought studies. *Environmental Research Letters* **2019**, *14*.
55. Anyamba, A.; Tucker, C.J.; Eastman, J.R. Ndvi anomaly patterns over africa during the 1997/98 enso warm event. *International Journal of Remote Sensing* **2001**, *22*, 1847-1859.
56. Bogardi, I.; Matyasovszky, I.; Bardossy, A.; Duckstein, L. A hydroclimatological model of areal drought. *Journal of Hydrology* **1994**, *153*, 245-264.